

Determining the maximum information gain and optimising experimental design in neutron reflectometry using the Fisher information

James H. Durant¹, Lucas Wilkins², Keith Butler³, and Joshaniel F. K. Cooper¹

¹ISIS Neutron and Muon source, Rutherford Appleton Laboratory, Harwell Campus, OX11 0QX

²Department of Zoology, University of Oxford, Mansfield Road, Oxford, OX1 3SZ

³SciML, Scientific Computing Division, Rutherford Appleton Laboratory, Harwell Campus, OX11 0QX

Abstract

An approach based on the Fisher information metric (FIM) is developed to quantify the maximum information gain and optimal experimental design in neutron reflectometry experiments. In these experiments, the FIM can be analytically calculated and used to provide sub-second predictions of parameter uncertainties. This approach can be used to influence real-time decisions about measurement angle, measurement time, contrast choice and other experimental conditions based on parameters of interest. The FIM provides a lower bound on parameter estimation errors. These are shown to decrease with the square root of measurement time, providing useful information for the planning and scheduling of experimental work. As the FIM is computationally inexpensive to calculate, it can be computed repeatedly during the course of an experiment, saving costly beam time by signalling that sufficient data has been obtained; or saving experimental datasets by signalling that an experiment needs to continue. The approach's predictions are validated through the introduction of an experiment simulation framework that incorporates instrument specific incident flux profiles, and through investigation of the specific case of measuring the structural properties of a phospholipid bilayer.

1 Introduction

The Fisher information metric (FIM) [Fisher, 1925] has been applied across many fields, from information theory and communications [Wang and Yin, 2010, Barnes et al., 2019] to quantum mechanics [Barndorff-Nielsen and Gill, 2000, Petz, 2002], quantitative finance [Taylor, 2019] and volcanology [Telesca et al., 2009]. The metric provides a way of measuring the amount of information an observable variable carries about an unknown parameter of a distribution that models the observable. For certain situations, it is possible to analytically calculate the FIM, giving a measure of parameter uncertainty, as well as inter-parameter correlations. Neutron reflectometry allows one to model a measured reflectivity curve, in order to determine the properties of the thin film layer structure that produced the curve. Most reflectometry analyses use sampling methods to extract parameter uncertainties, though this is expensive and cannot be performed in real time with current software [Nelson and Prescott, 2019, Kienzle et al., 2017, Hughes, 2017]. In this paper, we describe an application of the FIM to neutron reflectivity in enabling near real time estimation of parameter

uncertainties, as well as a projection of these with time. We compare the results to established sampling methods and demonstrate the FIM’s use for experimental design, and for potentially enabling early stopping of experiments based on counting statistics.

In reflectivity, a thin film is described by a thickness, a scattering length density (SLD) which is the product of the neutron scattering length and the film density, and an interfacial roughness. Thin film heterostructures are composed of multiple thin films on top of each other. In the analysis of reflectometry data, we are presented with data points of reflectivity, r , as a function of momentum transfer, Q , and wish to infer the SLD profile from the top surface to the substrate. For a single interface, i.e. a semi-infinite substrate, the neutron reflectivity decays $\sim Q^{-4}$, also called the Fresnel reflectivity. A single layer on a substrate is analytically solvable [Sivia, 2013], however, for more layers, multiple reflections are possible, and the inversion of the curve to a SLD profile is non-trivial. In fact, the loss of phase information upon reflection makes inversion of the SLD profile from the reflectometry profile an inverse problem [Majkrzak and Berk, 1995] and approximations are required.

Typically, reflectometry analysis is model-dependent where a model is defined using series of contiguous layers and the model reflectivity is calculated using the Abelès matrix formalism for stratified media [Abelès, 1948] or Parratt recursive method [Parratt, 1954]. However, the solution to this analysis is not necessarily unique and often requires *a priori* knowledge such as details of a system or the underlying science. Such prior knowledge helps to limit the dimensionality of the optimisation space by reducing the number of structures that agree with the experimental data within some tolerance. Methods have been devised to estimate interface properties, using this prior knowledge, that describe the data while adhering to a given set of constraints. Such methods include optimisers applying gradient projection [Byrd et al., 1995], annealing processes [Xiang et al., 1997], and evolutionary algorithms [Storn and Price, 1997].

Another approach to optimisation is the use of sampling methods of which there are two discussed in this paper, Metropolis-Hastings Markov Chain Monte Carlo (MCMC) [Metropolis et al., 1953, Hastings, 1970] and nested sampling [Skilling, 2004, Skilling, 2006], both of which are Bayesian and sample the parameter posterior distribution. Due to the typically high dimensionality of the parameter space in reflectometry, Bayesian sampling methods tend to be computationally expensive and impractical for obtaining results, such as parameter estimates and covariances, in real-time. In this paper, we use **refnx** [Nelson and Prescott, 2019] MCMC and **dynesty** [Speagle, 2019] nested sampling to sample our data and to compare the results to those derived from the FIM; **refnx** uses the **emcee** package [Foreman-Mackey et al., 2012] to provide an implementation of an invariant MCMC ensemble sampler [Goodman and Weare, 2010].

Much work has been undertaken on quantifying the information content of a reflectivity dataset, with most applying Bayesian statistics, where probability represents a degree-of-belief or plausibility based on the evidence at hand [Sivia and Skillings, 2012]. One such approach, looked at experimental optimisation by determining the information gain from a given experiment using the entropies of the posterior and prior probability density functions [Treece et al., 2019]. Similarly, work has been done on quantifying the information gain from scattering experiments as a function of the scattering length density of molecular components [Heinrich et al., 2020]. Many other Bayesian information-based approaches have been applied to reflectometry including the use of Bayesian evidence to determine the set of free parameters that maximise model information density [McCluskey et al., 2020], and using maximum entropy to reconstruct a SLD profile from a

reflectivity curve [Sivia et al., 1991].

Similarly to previous works, we propose a methodology for quantifying the information content of a reflectivity dataset for use in determining maximum information gain and experimental design optimisation. However, we attempt to solve a slightly different problem to previous work as, for our application, the error bars on our reflectivity points are defined as the square root of the number of neutron counts and these counts are governed by Poisson statistics. Under these assumptions, we can analytically calculate the FIM and apply the Cramér-Rao bound [Cramér, 1946, Rao, 1994]. The bound that states the inverse of the FIM provides a strict lower bound on the variance of an observable variable and, as consequence, the FIM provides us with a strict upper bound on the amount of information extractable from the observable. In practice, using this analytical derivation, we can achieve sub-second calculations of parameter uncertainties.

2 Methods

2.1 Derivation

To derive the equations for information content quantification using the FIM, we must first provide a structure for given reflectivity data of N points (or, equivalently histogram bins). This structure consists of contiguous layers representing a physical sample with each layer being defined by its thickness, SLD and interfacia roughness. A model is then described by this structure and given measurement background noise, experimental scale factor, and instrument resolution; we need only vary the M unknown parameters of this model. Such a model describes the reflectance at a given neutron momentum transfer, for example, using the Abelès matrix formalism implemented in **refnx**. Please refer to the supplementary information (SI) for the full derivation but, in summary, the Fisher information, \mathbf{g}^ξ , about the M parameters, ξ , of a model of N reflectivity points, is given by

$$\mathbf{g}^\xi = \mathbf{J}^T \mathbf{M} \mathbf{J} \quad (1)$$

where \mathbf{J} is the Jacobian of the reflectances, r_i , with respect to the parameters, ξ and \mathbf{M} is a diagonal matrix of incident counts, s_i divided by model reflectances r_i .

$$\mathbf{J} = \begin{bmatrix} \frac{\partial r_1}{\partial \xi_1} & \frac{\partial r_1}{\partial \xi_2} & \cdots & \frac{\partial r_1}{\partial \xi_M} \\ \frac{\partial r_2}{\partial \xi_1} & \frac{\partial r_2}{\partial \xi_2} & \cdots & \frac{\partial r_2}{\partial \xi_M} \\ \vdots & \vdots & \ddots & \vdots \\ \frac{\partial r_N}{\partial \xi_1} & \frac{\partial r_N}{\partial \xi_2} & \cdots & \frac{\partial r_N}{\partial \xi_M} \end{bmatrix} \quad (2) \quad \mathbf{M} = \begin{bmatrix} s_1/r_1 & 0 & \cdots & 0 \\ 0 & s_2/r_2 & \cdots & 0 \\ \vdots & \vdots & \ddots & \vdots \\ 0 & 0 & \cdots & s_N/r_N \end{bmatrix} \quad (3)$$

2.2 Experiment Simulation

To simulate an experiment, we require both a model and knowledge of the flux of incident neutrons as a function of wavelength. In our case, this was taken on the OFFSPEC reflectometer [Dalgliesh et al., 2011]. We can multiply this incident neutron flux by a constant in order to change the experimental counting time and to give us the number of incident neutrons for a simulated experiment; this approach was developed from the ideas presented by [Mironov et al., 2021]. To account for different measurement angles we multiply this incident flux by a factor to compensate

for different slit openings. Since both of the slits that are used to define the beam footprint scale as the angle, we scale intensity as the square of the angle.

We then calculate the momentum transfer, Q , for each wavelength in the file using the measurement angle, θ , and equation

$$Q = \frac{4\pi \sin \theta}{\lambda}$$

These Q values are assigned to geometrically spaced bins, with the number of bins being set to the desired number of points for the simulated dataset.

Following this, we iterate over each bin, i , and calculate the bin's centre, Q_i . Next, the model reflectivity for the bin, r_i , is calculated using **refnx** and is multiplied by the bin's incident flux, μ_i , to obtain the reflected flux. Additive instrument background noise, α , is added and the resulting value is multiplied by the measurement time, τ , to get the reflected counts for the bin. We then use the reflected counts as the λ parameter of a Poisson distribution which we then take a random value from, giving us an appropriately randomised number of reflected counts, N_i .

$$N_i \sim \text{Poisson}(\lambda) \text{ where } \lambda = (r_i \mu_i + \alpha) \tau$$

The bin's standard error in count-space is then just the square root of this value, $\sqrt{N_i}$. To obtain the reflectivity and associated error, we simply divide the “noisy” counts and associated error by the number of incident neutrons for the bin, s_i (I.e. the product of the bin's incident flux and measurement time, $\mu_i \tau$).

2.3 Applying the Fisher Information Metric

The FIM can be applied to both measured and simulated experimental data. As the Fisher information measures the instrumental uncertainty relative to changes in model parameters, a parameterised model must be provided and parameter values input. These parameter values can be obtained as estimates based on data, or specified manually if the task is simply the verification of a particular structure.

In this paper, we use **refnx** to define a model and to load the model's associated measured or simulated reflectivity data. The parameters of the model are then optimised using a fitting algorithm of choice, in our case differential evolution [Storn and Price, 1997], according to the χ^2 distance or equivalently, the negative log-likelihood. The likelihood provides a measure of difference between a given dataset and model and, for this work, is defined as its implementation in **refnx**

$$-\ln \mathcal{L} = \frac{1}{2} \sum_{i=1}^N \left(\left(\frac{r_i - r_{i_m}}{\delta r_i} \right)^2 + \ln [2\pi(\delta r_i)^2] \right)$$

where, N is the number of measured Q points, r_i is the experimental reflectivity at the i th Q point, δr_i is the uncertainty in the experimental reflectivity at the i th Q point and r_{i_m} is the model reflectivity at the i th Q point calculated using the Abelès matrix formalism.

From here on, we no longer need the data, since the model and Poisson statistics describe the data sufficiently. Next, we calculate the Jacobian matrix of equation 2, whose entries are the gradient of the model reflectivity, r_i , with respect to each of the model parameters, ξ_j . We estimate this by

using a finite difference approximation based on the reflectance for parameter values 0.5% either side of the input value. Using this and the diagonal matrix, \mathbf{M} , of incident counts divided by model reflectances, we can calculate the FIM matrix using equation 1. Since, the calculation of this matrix is relatively simple, implementation for use in other fitting software [Kienzle et al., 2017, Hughes, 2017, Björck and Andersson, 2007] is straightforward.

The FIM matrix, \mathbf{g}^ξ , contains all of the information about parameter variances and covariances but these values require extraction. For a single parameter’s error bar, ϵ , the FIM is just the inverse of the variance, so we say

$$\epsilon = \sqrt{1/g^\xi}$$

To obtain the errors for multiple parameters, we take the square root of the inverse of the diagonal elements of the FIM matrix and to extract the covariance between any two parameters, we can calculate a confidence ellipse of given size k standard deviations (see SI for details).

2.4 Application to Soft Matter

To illustrate the utility of the FIM, we applied it to an experiment measuring a common model system for structural biology: a 1,2-dimyristoyl-*sn*-glycero-3-phosphocholine (DMPC) bilayer deposited onto a silicon surface. The lipids were measured against two water contrasts, H_2O and D_2O . The data was taken using the CRISP neutron reflectometer [Penfold et al., 1987] as part of the ISIS neutron training course and simultaneously fit using `RasCAL` [Hughes, 2017]. This fitting was constrained against measured data for bare SiO_2 coated with a $\text{Si}/\text{D}_2\text{O}$ interface.

Our model for the bilayer was defined by two lipid leaflets with fixed surface coverage. The model was fitted by area per molecule rather than volume fractions to avoid ambiguity arising from differing total molar quantities of headgroup and tailgroup components. The model also accounted for the headgroups and tailgroups containing water through defects across their surfaces and also the water bound to the hydrophilic headgroups. The full details of the bilayer model parameterisation and fitting can be found in the SI. After fitting, we re-paramaterised the bilayer model as a function of contrast SLD and using this model, were able to simulate the DMPC bilayer experiment on the OFFSPEC reflectometer with arbitrary contrast SLD. We then investigated the change in the FIM, for each layer thickness and roughness, with increasing contrast SLD.

3 Results and Discussion

3.1 Measured vs. Simulated Data

To demonstrate the robustness of our experiment simulation, we compare a dataset measured using the OFFSPEC neutron reflectometer to its simulated counterpart. This data was measured using angles 0.3° , 0.4° , 0.5° , 0.6° , 0.7° and 2.0° with measurement times of 1.5 minutes per angle. To obtain a “ground truth” model for simulation, we fitted this data using `refnx` to get table 1. The background, experimental scale factor and resolution used for fitting were 8×10^{-7} , 0.783, and 2.5% dQ/Q respectively. For each measurement angle, we used the same angle, counting time and number of points for the simulation.

As can be visually seen in figure 1, the noise characteristics of the measured and simulated data are very similar. Statistically, comparing the datasets we find using the Hotelling’s t^2 test $p = 0.874$ and $t^2 = 0.159$, Anscombe Transformed [Hotelling, 1931, Anscombe, 1948], implying no significant differences between the measured and simulated data.

	SLD (10^{-6}\AA^{-2})	Thickness (\AA)	Roughness (\AA)
Layer 1 (Si)	1.795	790.7	24.5
Layer 2 (Cu)	6.385	297.9	3.50
Substrate (Quartz)	3.354	N/A	12.9

Table 1: Fitted SLD, thickness and roughness values for each layer of the model for the measured dataset.

3.2 Benchmarking

As mentioned previously, the FIM approach has notable performance upsides. To demonstrate this, we compared the time to obtain parameter uncertainties using the approach and using established Bayesian methods, given a correct and fitted model. For FIM-derived results to be useful, the given model needs to be correct and so if model selection is required, the performance gains of our approach could be lessened.

The benchmark was run on a CPU with no methods having multiprocessing explicitly enabled. MCMC sampling was run with a 400 step burn-in period followed by a 30 step sample with each sample being separated by 100 iterations. Nested sampling was run using the default `dynesty` stopping criteria which is optimised for evidence estimation [Speagle, 2019]. Uniform priors were used with a 25% bound above and below the ground truth for each parameter. Following this, we ran our FIM approach on the same samples. Table 2 compares the mean processing times of 10 samples for each number of layers and, as can be clearly seen, the FIM approach is significantly faster. It should be noted that our implementation is not particularly optimised and we believe further performance gains could be obtained if they were required.

For each number of layers in the interval $[1, 6]$, we randomly generated 10 samples and varied the SLD, thickness and interfacial roughness of each layer in each sample. Each sample used a silicon substrate of $\text{SLD } 2.047 \times 10^{-6}\text{\AA}^{-2}$ and the random SLD, thickness and roughness of each layer were sampled from uniform distributions of intervals $[-1, 10] \times 10^{-6}\text{\AA}^{-2}$, $[20, 1000] \text{\AA}$ and $[2, 8] \text{\AA}$ respectively. Using our experiment simulation, we synthesised data for each of these samples and ran both MCMC and nested sampling to obtain parameter uncertainties. Each experiment simulation consisted of 140 points obtained from two angles, 0.7° and 2.0° , using simulated measurement times of 7.5 and 30 minutes respectively. Background noise of 10^{-6} , instrument resolution of $2\% dQ/Q$ and experimental scale factor of 1.0 were used.

3.3 Corner Plots and Confidence Ellipses

In `refnx` and `dynesty`, the results of MCMC and nested sampling respectively can provide a corner plot which is “an illustrative representation of different projections of samples in high dimensional spaces” [Foreman-Mackey, 2016]. These Bayesian sampling methods sample the parameter posterior

No. Layers	No. Parameters	Calculation Time (s)					
		MCMC Sampling		Nested Sampling		FIM Approach	
		Mean	SD	Mean	SD	Mean	SD
1	3	197.83	3.34	53.31	8.95	0.23	0.02
2	6	229.64	5.03	155.48	35.92	0.56	0.04
3	9	262.57	5.33	363.32	120.07	0.96	0.04
4	12	292.38	3.24	1968.57	124.74	1.40	0.03
5	15	330.58	9.53	2967.71	561.53	1.92	0.09
6	18	372.12	5.67	3862.19	700.43	2.57	0.08

Table 2: Calculation time of parameter uncertainties, in seconds, for MCMC sampling, nested sampling and the FIM approach. For each number of layers, 10 samples were randomly generated using that number of layers with the mean and standard deviation of the calculation time recorded for each approach.

distribution, allowing contours to be drawn through samples that are equally probable. The FIM, however, is developed from a frequentist view and the confidence ellipses bound regions where we have at least a $k\sigma$ confidence of the value. Despite these fundamental differences, the sampling corner plots do still often agree very closely with the FIM confidence ellipses.

For samples with mostly uncorrelated parameters, we found that the corner plots showed strong agreement with the confidence ellipses. However, when more parameter correlation was present, the sampling uncertainties were much larger and we reach a point at which the FIM still represents the maximum obtainable information, but this seemingly cannot be extracted from the experimental data. As consequence, the confidence ellipses do not match the corner plots as closely. This discrepancy is shown in figure 2 which compares two samples: a simple sample with mostly uncorrelated parameters and a more complicated sample with more parameter correlation due to similar layer SLDs. The datasets of figure 2 were both simulated with the same run condition as as detailed above.

One potential source of deviation between corner plots and confidence ellipses may come from our fitting algorithm of choice. For our application of the FIM, our estimator is a fitting algorithm and, so far, we have assumed that this estimator is unbiased. Thus, the Cramér-Rao bound implies that the inverse of the FIM is a lower bound on the variance of this estimator. However, in practice, we found that our fitting algorithm of choice, differential evolution in `refnx`, may exhibit bias in some cases. To measure this bias, we simulated 1000 experiments, using the same simulation setup as above, for a number of different samples of varying complexity, and calculated the difference between the “ground truth” and mean fitted parameter values. We found evidence of some fitting bias and that the fitting bias was particularly evident in the presence of large parameter correlations; these biases are model dependent and potentially fitting package dependent.

The Cramér-Rao bound may be modified for a biased estimator, however for a real measurement there is no way to be able to tell if such a bias exists. As such, we leave our approach with the stricter limit (since any bias always increases the variance), and remind ourselves that the maximum possible information contained in the data is not always going to be the maximum extractable from the data.

3.4 Time Dependence

One potential use of the FIM in reflectometry is enabling early stopping of experiments based on counting statistics. To determine the feasibility of this application and to validate our implementation, we investigated how parameter errors change with measurement time. As derived in the SI, we should expect the error bar on a parameter, ϵ , to be inversely proportional to the square root of the experiment measurement time, τ . By using the fact that $\epsilon \propto 1/\sqrt{\tau}$, introducing a non-zero proportionality constant, α , and taking the natural logarithm of both sides we see

$$\begin{aligned}\ln \epsilon &= \ln \frac{\alpha}{\sqrt{\tau}} \\ &= \ln \alpha - \ln \sqrt{\tau} \\ &= -\frac{1}{2} \ln \tau + \ln \alpha\end{aligned}$$

Using this result, we should expect the gradient of the plot of log parameter error, $\ln \epsilon$, vs. log time, $\ln \tau$, to be $-\frac{1}{2}$. To confirm this is the case, we compared established fitting error measures and errors derived from the FIM with increasing time using our experiment simulation. Using simple linear regression, we found that the time dependence for any one error bar was indeed determined by the square root of the measurement time as is shown in figure 3. We used the same simulation parameters and samples as those used in figure 2 and, for the simple sample, the relationship is perfectly exhibited. For the more complicated sample, the relationship can still be seen albeit the results are slightly more noisy due to the increased difficulty of fitting. This is particularly noticeable when the counting time is low and the data being fitted is significantly impacted by our added noise. However, since we now know that the parameter error uncertainty decreases as the square root of the measurement time we are able to easily project the evolution of the uncertainty and can predict when it would reach some threshold, at which we may want to cease the measurement.

3.5 Application to Soft Matter

As detailed previously, we applied our FIM-based approach to a soft matter experiment. The FIM was calculated for each model parameter of the DMPC bilayer as a function of bulk water contrast SLD from $-0.56 \times 10^{-6} \text{\AA}^{-2}$ to $6.35 \times 10^{-6} \text{\AA}^{-2}$ (pure H₂O to pure D₂O). The fitted SLD profiles and experimental reflectivity data are shown in figure 4 together with the FIM for each parameter. As might naively be expected, we show that it is possible to extract more information about some parameters than others. This result is certainly no surprise for researchers in the field who have experience fitting this system, but it does allow us to quantify it. Additionally, we show that the information gain as a function of contrast is non-monotonic, almost certainly due to hydration of various components leading to them becoming indistinguishable from neighbouring components for some bulk water deuterium concentrations. Due to the way we have parameterised our model, the bilayer model roughness is better defined (higher information content) than the other system roughnesses. This is likely to be because it is shared between all the lipid layers, effectively increasing its information weighting.

Figure 4 also indicates that the greatest information gain is almost always obtainable from the highest SLD water, D₂O. It is well established that measuring multiple contrasts will reduce parameter

uncertainties and so this result may seem unusual. However, we believe that the benefit of measuring multiple contrasts comes from reducing inter-parameter correlations. Recalling that highly correlated parameters are more difficult to extract information from, having multiple contrasts for the same parameters allows one to better decouple these correlations. While difficult to display, if you have a model, it would be possible to calculate the optimal contrasts to measure in order to minimise correlations. The optimal solution is almost certainly model dependent, but given the broad features found here, it is unlikely to be an issue having a slightly incorrect model.

4 Future Work

The approach presented in this paper has many potential applications in neutron reflectometry, and other techniques based on counting statistics. As demonstrated by our soft matter application, experimental design is one such use where the FIM could be used to influence real-time decisions of measurement angle and/or contrast choice; a similar Bayesian approach would be infeasible for real-time application due to computational overhead. On a closely related note, we believe the FIM could be used to quantify how much new information could be gained from a chosen contrast or measurement angle given prior measured data of the same sample. Such a tool would allow for optimal experimental setups to be determined and could give insight as to why particular experimental design choices have found popularity throughout the literature.

As discussed, the FIM uncertainties do not always match those obtained from established methods and so, with such an application, it could be worthwhile providing experimenters with a “usefulness” metric. As fitting is required before calculating the FIM, the metric could be derived from fitting errors.

5 Conclusions

In this paper, we presented a framework for determining maximum information gain and experimental design optimisation in neutron reflectometry using the the FIM. We demonstrated how the FIM allows us to quantify the information content of a measured data point in relation to given model parameters. To illustrate this point, we simulated experimental datasets with realistic noise characteristics to compare the FIM results to Bayesian sampling methods. Despite the potential differences in FIM and sampling uncertainties, we believe this approach has significant upsides in its run time. By using the fact that our experimental data points can be treated independently and that their errors are Poisson, we can analytically calculate the FIM and minimise computational overhead as demonstrated in our benchmark. We emphasise that this provides an upper bound on the amount of extractable information and not necessarily the information extracted in practice due to inter-parameter correlations and fitting biases. Finally, we demonstrated a practical application of the approach in determining the information content of the parameters of a DMPC bilayer sample parameterised as a function of bulk water contrast SLD.

The code for this work is open source and freely available on GitHub [Durant et al., 2021].

6 Acknowledgements

This work has been partially supported by the STFC Facilities Programme Fund through the ISIS Neutron and Muon Source, and Scientific Computing Department of Rutherford Appleton Laboratory, Science and Technology Facilities Council, and by the Wave 1 of The UKRI Strategic Priorities Fund under the EPSRC Grant EP/T001569/1, particularly the “AI for Science” theme within that grant and The Alan Turing Institute. We would also like to thank Luke Clifton for his assistance and expertise in fitting the DMPC data.

References

- [Abelès, 1948] Abelès, F. (1948). Sur la propagation des ondes électromagnétiques dans les milieux stratifiés. *Annales de Physique*, 12(3):504–520.
- [Anscombe, 1948] Anscombe, F. J. (1948). The transformation of Poisson, binomial and negative-binomial data. *Biometrika*, 35(3–4):246–254.
- [Barndorff-Nielsen and Gill, 2000] Barndorff-Nielsen, O. E. and Gill, R. D. (2000). Fisher information in quantum statistics. *Journal of Physics A: Mathematical and General*, 33(24):4481–4490.
- [Barnes et al., 2019] Barnes, L. P., Han, Y., and Özgür, A. (2019). Fisher Information for Distributed Estimation under a Blackboard Communication Protocol. In *IEEE International Symposium on Information Theory - Proceedings*, pages 2704–2708. Institute of Electrical and Electronics Engineers.
- [Björck and Andersson, 2007] Björck, M. and Andersson, G. (2007). GenX: An extensible X-ray reflectivity refinement program utilizing differential evolution. *Journal of Applied Crystallography*, 40(6):1174–1178.
- [Byrd et al., 1995] Byrd, R. H., Lu, P., Nocedal, J., and Zhu, C. (1995). A limited memory algorithm for bound constrained optimization. *SIAM Journal of Scientific Computing*, 16(5):1190–1208.
- [Cramér, 1946] Cramér, H. (1946). *Mathematical methods of statistics*. Princeton University Press, Princeton.
- [Dalgliesh et al., 2011] Dalgliesh, R. M., Langridge, S., Plomp, J., de Haan, V. O., and van Well, A. A. (2011). Offspec, the ISIS spin-echo reflectometer. *Physica B: Condensed Matter*, 406(12):2346–2349.
- [Durant et al., 2021] Durant, J. H., Wilkins, L., Butler, K., and Cooper, J. F. K. (2021). fisher-information. Available at: <https://github.com/James-Durant/fisher-information>. (Accessed: 27 January 2021).
- [Fisher, 1925] Fisher, R. A. (1925). Theory of Statistical Estimation. *Mathematical Proceedings of the Cambridge Philosophical Society*, 22(5):700–725.
- [Foreman-Mackey, 2016] Foreman-Mackey, D. (2016). corner.py: Scatterplot matrices in Python. *The Journal of Open Source Software*, 1(2):24.

- [Foreman-Mackey et al., 2012] Foreman-Mackey, D., Hogg, D. W., Lang, D., and Goodman, J. (2012). emcee: The MCMC Hammer. *Publications of the Astronomical Society of the Pacific*, 125(925):306–312.
- [Goodman and Weare, 2010] Goodman, J. and Weare, J. (2010). Ensemble samplers with affine invariance. *Communications in Applied Mathematics and Computational Science*, 5(1):65–80.
- [Hastings, 1970] Hastings, W. K. (1970). Monte carlo sampling methods using Markov chains and their applications. *Biometrika*, 57(1):97–109.
- [Heinrich et al., 2020] Heinrich, F., Kienzle, P. A., Hoogerheide, D. P., and Lösche, M. (2020). Information gain from isotopic contrast variation in neutron reflectometry on protein-membrane complex structures. *Journal of Applied Crystallography*, 53(3):800–810.
- [Hotelling, 1931] Hotelling, H. (1931). The Generalization of Student’s Ratio. *Annals of Mathematical Statistics*, 2(3):360–378.
- [Hughes, 2017] Hughes, A. V. (2017). RasCAL SourceForge. Available at: <https://sourceforge.net/projects/rscl>. (Accessed: 27 January 2021).
- [Kienzle et al., 2017] Kienzle, P. A., Maranville, B. B., O’Donovan, K. V., Ankner, J. F., Berk, N. K., and Majkrzak, C. F. (2017). NCNR Reflectometry Software. Available at: <https://www.nist.gov/ncnr/data-reduction-analysis/reflectometry-software>. (Accessed: 27 January 2021).
- [Majkrzak and Berk, 1995] Majkrzak, C. F. and Berk, N. F. (1995). Exact determination of the phase in neutron reflectometry. *Physical Review B*, 52(15):10827–10830.
- [McCluskey et al., 2020] McCluskey, A. R., Cooper, J. F. K., Arnold, T., and Snow, T. (2020). A general approach to maximise information density in neutron reflectometry analysis. *Machine Learning: Science and Technology*, 1(3):035002.
- [Metropolis et al., 1953] Metropolis, N., Rosenbluth, A. W., Rosenbluth, M. N., and Teller, A. H. (1953). Equation of state calculations by fast computing machines. *The Journal of Chemical Physics*, 21(6):1087–1092.
- [Mironov et al., 2021] Mironov, D., Durant, J. H., Mackenzie, R., and Cooper, J. F. K. (2021). Towards automated analysis for neutron reflectivity. *Machine Learning: Science and Technology*.
- [Nelson and Prescott, 2019] Nelson, A. R. J. and Prescott, S. W. (2019). refnx: neutron and X-ray reflectometry analysis in Python. *Journal of Applied Crystallography*, 52(1):193–200.
- [Parratt, 1954] Parratt, L. G. (1954). Surface studies of solids by total reflection of x-rays. *Physical Review*, 95(2):359–369.
- [Penfold et al., 1987] Penfold, J., Ward, R. C., and Williams, W. G. (1987). A time-of-flight neutron reflectometer for surface and interfacial studies. *Journal of Physics E: Scientific Instruments*, 20(11):1411–1417.
- [Petz, 2002] Petz, D. (2002). Covariance and fisher information in quantum mechanics. *Journal of Physics A: Mathematical and General*, 35(4):929–939.
- [Rao, 1994] Rao, C. R. (1994). *Selected papers of C.R. Rao*. Wiley, New York.

- [Sivia, 2013] Sivia, D. S. (2013). *Elementary Scattering Theory*. Oxford University Press.
- [Sivia et al., 1991] Sivia, D. S., Hamilton, W. A., and Smith, G. S. (1991). Analysis of neutron reflectivity data: maximum entropy, Bayesian spectral analysis and speckle holography. *Physica B: Condensed Matter*, 173(1):121–138.
- [Sivia and Skillings, 2012] Sivia, D. S. and Skillings, J. H. (2012). *Data analysis: a Bayesian tutorial*. Oxford University Press, second edition edition.
- [Skilling, 2004] Skilling, J. (2004). Nested Sampling. *AIP Conference Proceedings*, 735:395–405.
- [Skilling, 2006] Skilling, J. (2006). Nested sampling for general Bayesian computation. *Bayesian Analysis*, 1(4):833–860.
- [Speagle, 2019] Speagle, J. S. (2019). dynesty: a dynamic nested sampling package for estimating Bayesian posteriors and evidences.
- [Storn and Price, 1997] Storn, R. and Price, K. (1997). Differential Evolution - A Simple and Efficient Heuristic for Global Optimization over Continuous Spaces. *Journal of Global Optimization*, 11:341–359.
- [Taylor, 2019] Taylor, S. (2019). Clustering Financial Return Distributions Using the Fisher Information Metric. *Entropy*, 21(2):110.
- [Telesca et al., 2009] Telesca, L., Lovallo, M., Ramirez-Rojas, A., and Angulo-Brown, F. (2009). A nonlinear strategy to reveal seismic precursory signatures in earthquake-related self-potential signals. *Physica A: Statistical Mechanics and its Applications*, 388(10):2036–2040.
- [Treece et al., 2019] Treece, B. W., Kienzle, P. A., Hoogerheide, D. P., Majkrzak, C. F., Lösche, M., and Heinrich, F. (2019). Optimization of reflectometry experiments using information theory. *Journal of Applied Crystallography*, 52(1):47–59.
- [Wang and Yin, 2010] Wang, L. Y. and Yin, G. G. (2010). Quantized identification with dependent noise and fisher information ratio of communication channels. *IEEE Transactions on Automatic Control*, 55(3):674–690.
- [Xiang et al., 1997] Xiang, Y., Sun, D. Y., Fan, W., and Gong, X. G. (1997). Generalized simulated annealing algorithm and its application to the Thomson model. *Physics Letters, Section A: General, Atomic and Solid State Physics*, 233(3):216–220.

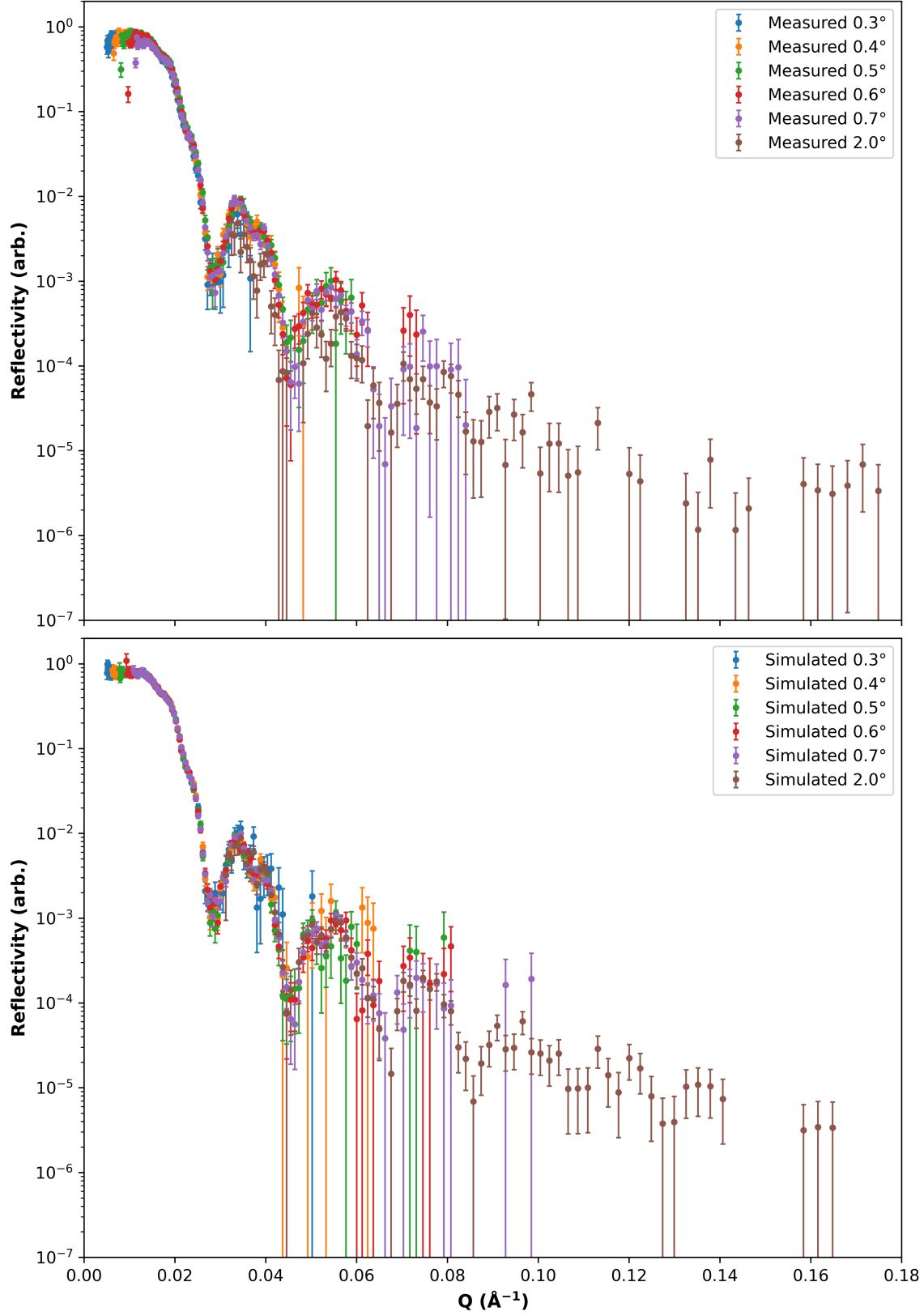


Figure 1: Measured reflectivity (top) and simulated reflectivity (bottom) vs. momentum transfer, Q , for each measurement angle of the table 1 sample.

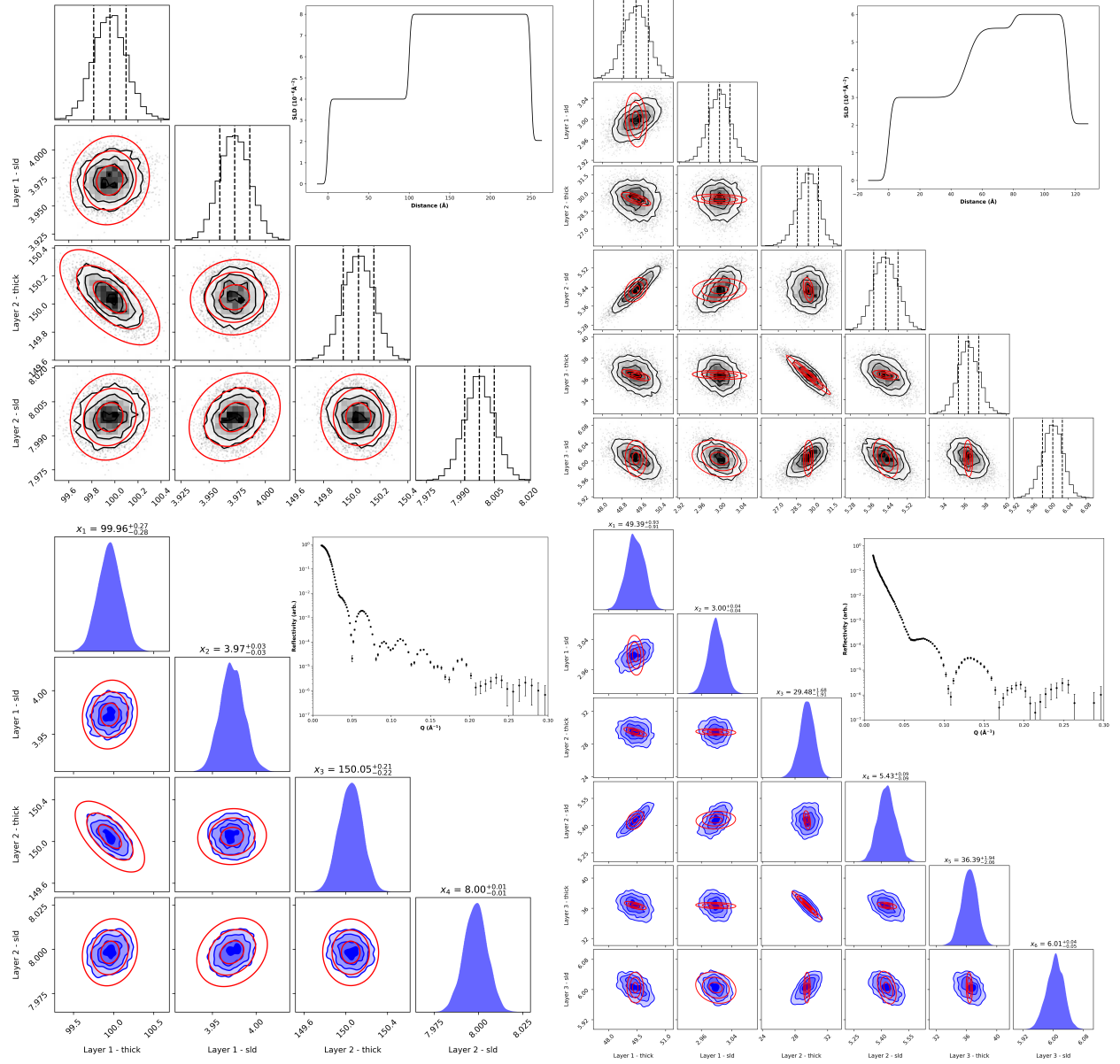


Figure 2: The FIM confidence ellipses for $k = 1, 2, 3$ (red) overlaid on the corner plots of MCMC (black) and nested sampling (blue) for the mostly uncorrelated parameter sample (left) and correlated parameter sample (right). Inset are the SLD profiles (top) and rebinned simulated reflectivity curves (bottom) of the two samples.

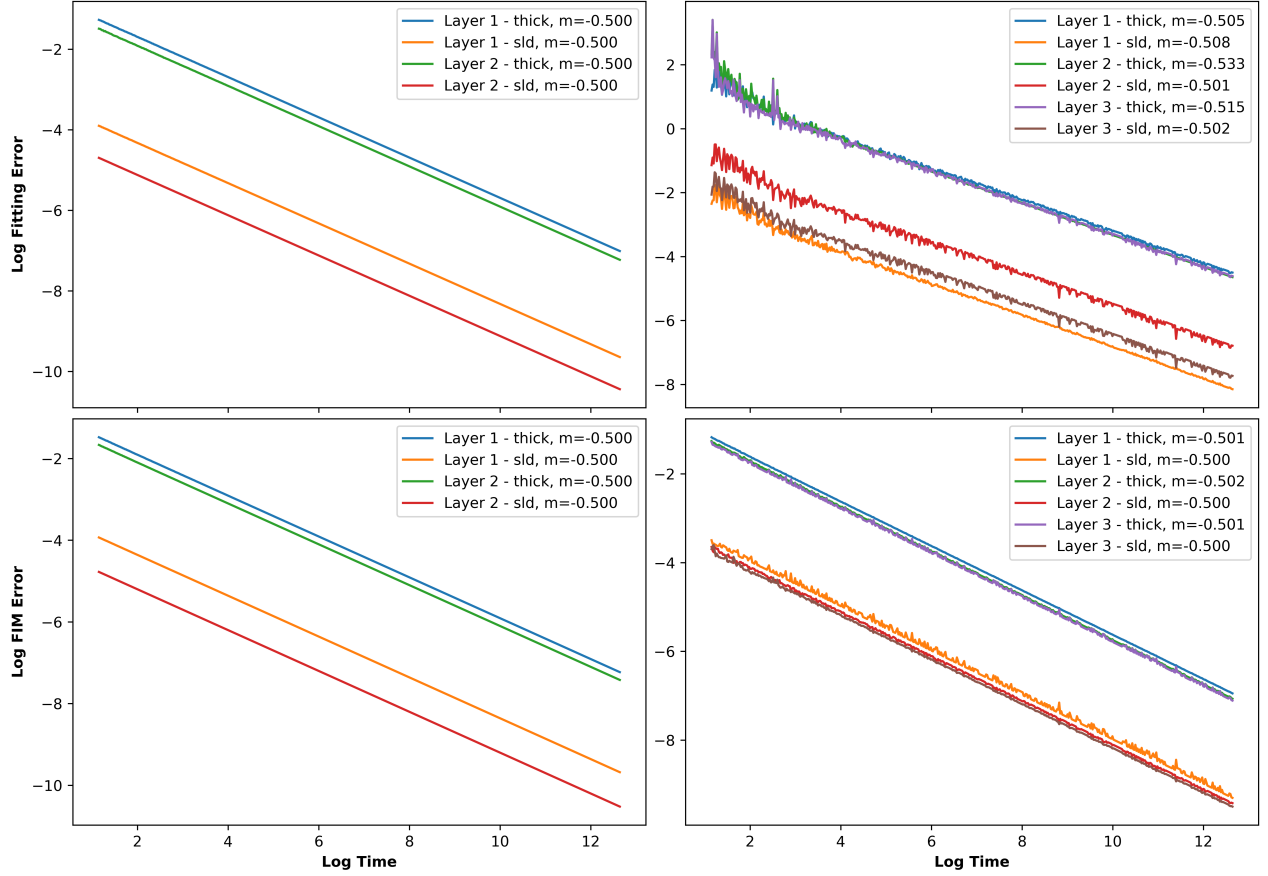


Figure 3: Log fitting errors (top) and log FIM errors (bottom) vs. log time for each parameter of the mostly uncorrelated parameter sample (left) and correlated parameter sample (right); the errors are taken as the mean from 10 simulated experiments for a given measurement time. Included in the legends are an approximation of the gradients of the lines, m , as given by linear regression.

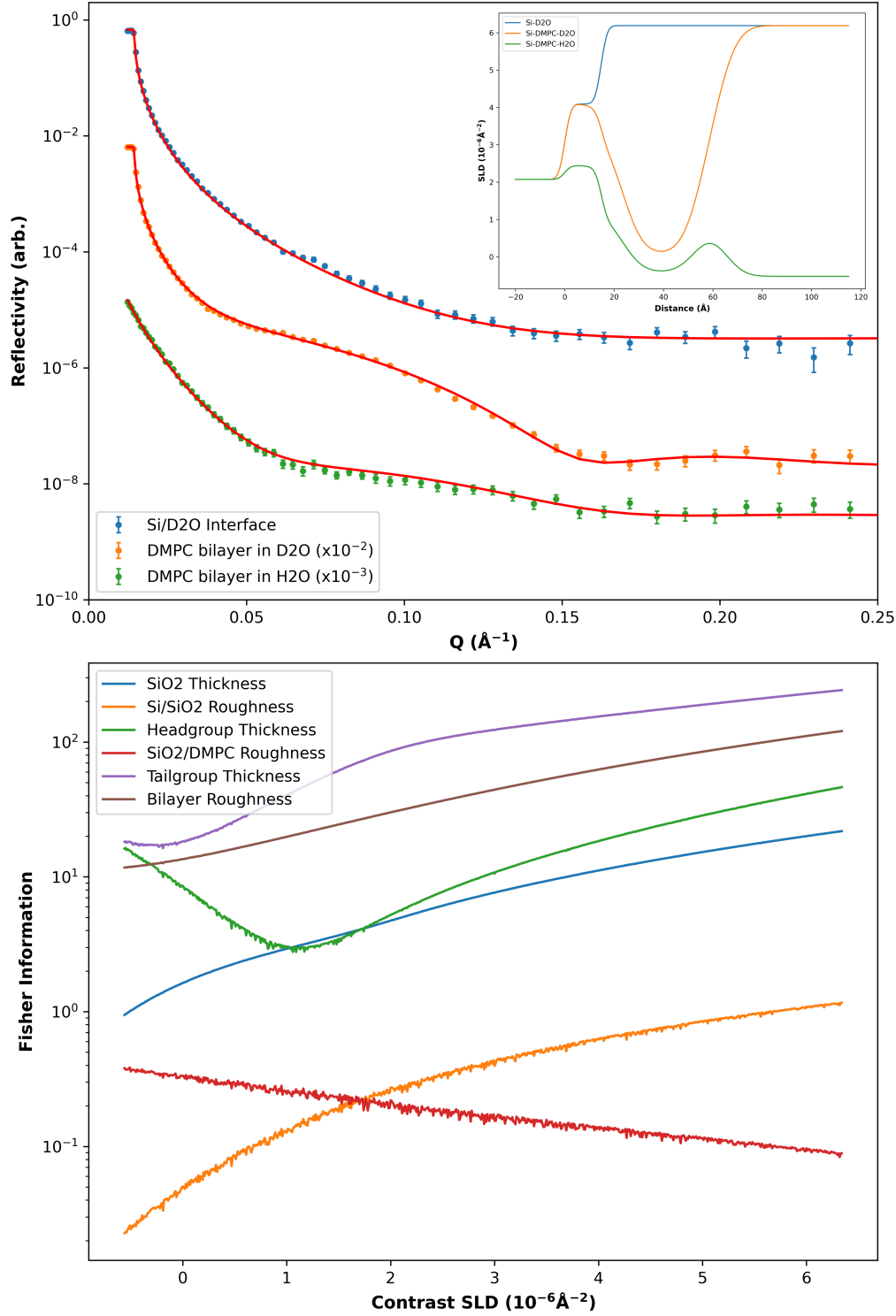


Figure 4: Fitted experimental reflectivity vs. momentum transfer (top) for the Si/D₂O interface and the two solution isotopic contrast datasets, H₂O and D₂O, offset for clarity by factors of 10^{-2} and 10^{-3} respectively. Inset are the corresponding fitted SLD profiles. Also shown (bottom) is the FIM for each for each model parameter as a function of the bulk water SLD, from H₂O to D₂O.

7 Supplementary Information

7.1 Deriving the Fisher Information

7.1.1 Notation

N	Number of bins or equivalently, data points
M	Number of model parameters
λ_i	Expected neutron counts in bin (parameter) i
$\lambda = (\lambda_1 \dots \lambda_N)$	Vector of expected neutron counts in all bins (parameter)
τ_θ	Time recording at experimental condition θ , e.g. angle, contrast
$\mu_{i\theta}$	Incident flux in bin i for condition θ (parameter)
g^z	Fisher information for parameterisation z
ξ_j	Parameters of the structure model
$r_i(\xi)$	Reflectance for bin i from model with parameters ξ
X	Random variable describing a full measurement of N points
$x_i \in \mathcal{X}_i$	Neutron count in bin i
$p(x; z)$	Probability distribution for measurements x , parameterised by z
$\Pr([\text{event}])$	Probability of event
s_i	Total number of incident neutrons in bin i

7.1.2 The Model

In reflectometry, a model describes the reflectance at a given neutron momentum transfer. These momentum transfer values are binned with the measured number of neutrons in bin i being given by

$$\lambda_i = r_i s_i(\tau) \quad (4)$$

where s_i is the number of neutrons incident in bin i . s_i is a function of the number of incident neutrons in the i th bin at each experimental condition, $\mu_{i\theta}$, and the time each condition is measured for τ_θ .

$$s_i(\tau) = \sum_k \tau_k \mu_{ik}$$

and so

$$\lambda_i(\xi) = \sum_\theta r_i(\xi) \tau_\theta \mu_{i\theta}$$

7.1.3 Fisher Information about the λ coordinates

The probability distribution of the measurement in one bin is Poisson distributed

$$\Pr(X_i = x_i; \lambda_i) = \frac{e^{-\lambda_i} \lambda_i^{x_i}}{x_i!}$$

and the corresponding Fisher information for this bin, with respect to λ_i , is

$$g^{\lambda_i} = 1/\lambda_i = 1/\mathbb{E}[\text{var } X_i]$$

The probability distribution for the whole measurement is, by independence

$$\Pr(X = (x_0 \dots x_N)) = \prod_i \Pr(X_i = x_i)$$

and the corresponding Fisher information with respect to λ is

$$g_{jk}^\lambda = \begin{cases} g^{\lambda_k} & \text{if } j = k \\ 0 & \text{otherwise} \end{cases}$$

i.e. a diagonal matrix with values of g^{λ_i} which happens to equal (in this case, but not in general), $\mathbb{E}[\text{cov } X]^{-1}$.

7.1.4 Fisher Information about the ξ coordinates.

In general, we can transform the Fisher information using tensor transforms, i.e.

$$g_{ij}^Z = g_{ab}^Y \frac{\partial y_a}{\partial z_i} \frac{\partial y_b}{\partial z_j}$$

So, the Fisher information in terms of ξ is just

$$g_{ij}^\xi = g_{ab}^\lambda \frac{\partial \lambda_a}{\partial \xi_i} \frac{\partial \lambda_b}{\partial \xi_j}$$

To get the Fisher information as a function of τ , we take the derivative of equation 4 with respect to ξ which gives us

$$\frac{\partial \lambda_i}{\partial \xi_j} = s_i(\tau) \frac{\partial r_i}{\partial \xi_j} \quad (5)$$

The derivative $\frac{\partial r_i}{\partial \xi_j}$ is obtained from the model alone (irrespective of the data); it is the derivative of the reflectance for bin i with respect to the j th ξ parameter.

We can now put everything together. First, we have the initial Fisher information about the λ parameter, which we can write in terms of s and r_i

$$\mathbf{g}^\lambda = \begin{bmatrix} 1/s_1 r_1 & 0 & \cdots & 0 \\ 0 & 1/s_2 r_2 & \cdots & 0 \\ \vdots & \vdots & \ddots & \vdots \\ 0 & 0 & \cdots & 1/s_N r_N \end{bmatrix}$$

Equation 5 can be re-written in matrix form in terms of a diagonal matrix \mathbf{S} and the Jacobian matrix, \mathbf{J} , for the N modelled reflectance points, with respect to the M parameters, ξ .

$$\mathbf{S} = \begin{bmatrix} s_1 & 0 & \cdots & 0 \\ 0 & s_2 & \cdots & 0 \\ \vdots & \vdots & \ddots & \vdots \\ 0 & 0 & \cdots & s_N \end{bmatrix}$$

$$\mathbf{J} = \begin{bmatrix} \frac{\partial r_1}{\partial \xi_1} & \frac{\partial r_1}{\partial \xi_2} & \cdots & \frac{\partial r_1}{\partial \xi_M} \\ \frac{\partial r_2}{\partial \xi_1} & \frac{\partial r_2}{\partial \xi_2} & \cdots & \frac{\partial r_2}{\partial \xi_M} \\ \vdots & \vdots & \ddots & \vdots \\ \frac{\partial r_N}{\partial \xi_1} & \frac{\partial r_N}{\partial \xi_2} & \cdots & \frac{\partial r_N}{\partial \xi_M} \end{bmatrix} \quad (6)$$

The tensor transformation of \mathbf{g}^λ in this notation is then

$$\mathbf{g}^\xi = (\mathbf{S}\mathbf{J})^T \mathbf{g}^\lambda (\mathbf{S}\mathbf{J}) = \mathbf{J}^T \mathbf{S} \mathbf{g}^\lambda \mathbf{S}\mathbf{J}$$

$$(M \times M) = (M \times N)(N \times N)(N \times N)(N \times N)(N \times M)$$

and the matrix $\mathbf{S} \mathbf{g}^\lambda \mathbf{S}$ is a composition of diagonal matrices, and is equal to

$$\begin{bmatrix} s_1/r_1 & 0 & \cdots & 0 \\ 0 & s_2/r_2 & \cdots & 0 \\ \vdots & \vdots & \ddots & \vdots \\ 0 & 0 & \cdots & s_N/r_N \end{bmatrix}$$

7.1.5 Summary

In summary, the Fisher information about ξ is given by

$$\mathbf{g}^\xi = \mathbf{J}^T \mathbf{M} \mathbf{J} \quad (7)$$

where, \mathbf{J} is the Jacobian of the reflectances, r_i , with respect to the parameters, ξ . \mathbf{M} is a diagonal matrix with entries $(s_0/r_0, s_1/r_1 \dots s_N/r_N)$ and s_i is the incident neutron flux, which depends on the experimental condition k and the time spent measuring it, τ_k

$$s_i(\tau) = \sum_k \tau_k \mu_{ik}$$

7.2 Confidence Ellipses

To calculate confidence intervals in the general case, we can find the set of parameters that differ from the estimate by a certain number of standard deviations. To do this we need to know the length of a vector in parameter space in terms of the number of standard deviations. This is what the Fisher information does (technically, it gives a linear approximation to the informational distance between distributions, but they are related). So, if we want to find a vector with a given length, k , we solve

$$k^2 = \Delta \xi^T \mathbf{g} \Delta \xi$$

It so happens that k in the above equation can be interpreted as “number of standard deviations”, so a 2σ error bar will have $k = 2$. In practice, it is useful to fix a direction, and calculate the magnitude of the vector needed to reach the threshold. i.e. let $\Delta \xi = \epsilon \hat{\Delta} \xi$ where $\hat{\Delta}$ denotes a

unit vector. Consider the 1-D case. $k^2 = \epsilon^2 g$, g is analogous to the inverse variance, so we have $k^2 = \epsilon^2/\sigma^2$, so, if we want to know where $\epsilon = 2\sigma$, we would have $k^2 = (2\sigma)^2/\sigma^2$, thus $k = 2$.

In 2-D, the unit vectors can be written as $(\sin \vartheta, \cos \vartheta)$. We can graphically solve the following

$$k^2 = \epsilon^2 \underbrace{\left([\sin \vartheta, \cos \vartheta] g^\xi \begin{bmatrix} \sin \vartheta \\ \cos \vartheta \end{bmatrix} \right)}_{\text{scalar}}$$

for ϵ over a sample of angles, θ , in $[0, 2\pi]$ by plotting the points $(\epsilon(\theta) \sin \theta, \epsilon(\theta) \cos \theta)$. The result is a confidence ellipse of size k between two chosen parameters.

7.3 Point Estimates vs Posterior Distributions

An estimator, usually written with a $\widehat{}$, is a function of sampled data that provides an estimation of a parameter. In frequentist statistics, one is concerned with the probability distributions of *estimators*, not of the parameters themselves (as would be the case in Bayesian statistics). The distribution of estimators often has a variance. When it does, and when it is unbiased, i.e.

$$\mathbb{E}[\hat{\xi}] = \xi$$

then it is related to the Fisher information by the Cramér-Rao bound:

$$\text{var } \hat{\xi} \gtrsim \frac{1}{N} (g^\xi)^{-1}$$

7.4 Time Dependence

If there is a single measurement condition, we have $s_i = \mu_i \tau$. Then, we see that τ is a factor of all the s_i 's and so of the matrix \mathbf{M} and thus of \mathbf{g}^ξ . We can therefore write $\mathbf{g}^\xi = \tau \mathbf{f}^\xi$. The size of an “error bar”, ϵ , at a threshold, k , in a direction, $\widehat{\Delta\xi}$, is given by

$$k^2 = (\epsilon \widehat{\Delta\xi}) g^\xi (\epsilon \widehat{\Delta\xi})$$

And so,

$$k^2 = (\epsilon \widehat{\Delta\xi}) \tau \mathbf{f}^\xi (\epsilon \widehat{\Delta\xi})$$

Hence $\epsilon \propto 1/\sqrt{\tau}$.

7.5 Bilayer Model Parameterisation

For the measured DMPC sample, each experimental dataset was recorded with an instrument resolution of 2%. The instrument backgrounds were 3.21×10^{-6} , 2.80×10^{-6} and 2.06×10^{-6} respectively.

The SLDs of the Si substrate and following SiO₂ layer were defined using known values of $2.073 \times 10^{-6} \text{\AA}^{-2}$ and $3.41 \times 10^{-6} \text{\AA}^{-2}$. From fitting, we obtained values of 14.7\AA and 24.5% for the SiO₂

layer's thickness and hydration. For both the Si/SiO₂ and SiO₂/DMPC interfacial roughnesses, we obtained 2.00Å; all other interfacial roughnesses shared a common parameter that was fitted as 6.57Å.

By using the fact that the molecular volumes of the headgroups and tailgroups are known and constant at 320.9Å³ and 783.3Å³, any changes in molecule surface area must be inversely proportional to the headgroup and tailgroup thicknesses. Therefore, we need only fit one parameter: the area per molecule (APM) at the surface. From the APM we can calculate the tailgroups thickness using the known volume.

$$\text{Thickness} = \frac{\text{Volume}}{\text{APM}} \quad (8)$$

From fitting the APM parameter, we obtained a value of 49.9Å². Also using the tailgroup volume, the SLD of the tailgroups can be calculated using the known tailgroup scattering length (SL) of -3.08×10^{-4} Å and equation

$$\text{SLD}(\rho) = \frac{\Sigma b}{\text{Volume}} \quad (9)$$

Both the headgroups and tailgroups contain water through defects across their surfaces but there is also water bound to the hydrophilic headgroups. The model accounted for these differing hydration types by varying two parameters: the total bilayer hydration and headgroup bound waters for which we obtained values of 7.37% and 3.59. The headgroup water SLs in H₂O and D₂O were calculated as the product of the bound waters parameter and the known SLs of -1.64×10^{-5} Å and 2.00×10^{-4} Å for the H₂O and D₂O solutions. Further, the product of the bound waters parameter and the known volume of water, 30.4Å³, yields the headgroup water volume. The headgroup thickness was calculated using the total headgroup volume (including bound water), APM parameter and equation 8. To determine the headgroup SLs in H₂O and D₂O we took the sum of the known headgroup SL of 6.41×10^{-4} Å and headgroup SL in H₂O and D₂O previously calculated. Finally, using the headgroup SL in each contrast and the calculated headgroup volume, we then calculated the SLD of the headgroup in each solution using equation 9.

We re-paramaterised the fitted model as a function of bulk water contrast SLD using the known SLD of the DMPC headgroups of 1.98×10^{-6} Å⁻² (if no hydrating water was present) and approximating the headgroup hydration at 27%.